TEM Imaging of Cluster Unit Dissolution from a Single Crystal of Tetra-n-butylammonium Fluoride Semiclathrate Hydrate for Latent-Heat Storage Material

Hironobu Machida[†], *Takeshi Sugahara*[‡,§], *Hideki Hata*[||], *Tomohiko Ueda*[||], *Tomoya Yamazaki*[⊥], *Yuki Kimura*[⊥,*]

[†] Solution Development Division, Electric Works Company, Panasonic Corporation, 3-1-1 Yagumonakamachi, Moriguchi, Osaka 570-8501, Japan

[‡] Division of Chemical Engineering, Department of Materials Engineering Science, Graduate School of Engineering Science, Osaka University, 1-3 Machikaneyama, Toyonaka, Osaka 560-8531, Japan

[§] Division of Energy and Photochemical Engineering, Research Center for Solar Energy Chemistry, Graduate School of Engineering Science, Osaka University, 1-3 Machikaneyama, Toyonaka, Osaka 560-8531, Japan

[||] Product Analysis Center, Panasonic Holdings Corporation, 1048 Kadoma, Kadoma, Osaka 571-8686, Japan

[⊥] Institute of Low Temperature Science, Hokkaido University, Kita-19, Nishi-8, Kita-ku, Sapporo 060-0819, Japan

KEYWORDS : in situ transmission electron microscopy, electron diffraction, moiré pattern, single crystal, cluster, crystal growth

ABSTRACT: A nonclassical phase-transition model in which clusters act as the growth units has gained acceptance, contrasting with the classical phase-transition model where atoms or molecules attach or detach individually. However, this cluster-based model for phase transitions has not been established in phase transitions of semiclathrate hydrates, latent-heat storage materials, in which cage structures form and dissociate at the crystal surface. Using liquid-cell transmission electron microscopy, we directly observed the dissociation behavior of a single crystal of tetra-*n*-butylammonium fluoride semiclathrate hydrate induced by electron-beam irradiation. Early dissociation stages showed moiré patterns, indicating that a 10–30 nm region of the crystal surface had transitioned to a metastable phase. Subsequently, spherical clusters, potentially responsible for the memory effect that facilitates recrystallization after dissociation, appeared without diffraction contrast attributable to crystal. These observations provide insights into nonclassical dissociation processes of hydrates to understand phase transition of latent-heat storage materials.

INTRODUCTION:

As typified by the dissolution/precipitation process, dissolution and crystallization are closely related. Other examples include the promotion of crystallization due to partial melting caused by periodic changes in supersaturation,[1] and the memory effect, which facilitates the recrystallization

of crystals after the dissociation of a hydrate.[2] Therefore, an understanding of the processes of dissolution [or dissociation for a (semi)clathrate hydrate] is directly linked to an understanding of the mechanism of crystallization.

Phase-transition technology has been used in various chemical engineering fields, for example in the commercial production of pharmaceuticals, chemicals, foods, advanced materials (such as nanomaterials or biomaterials), and electronic devices.[3–5] In particular, the formation of a crystalline seed in a process called nucleation is important in the initial stages of crystallization because crucial features of the resulting crystals, such as the crystalline structure, lattice orientation, particle size, size distribution, and chirality, are determined in the early stages of crystallization.[6–8] Moreover, competition between clusters with different structures is important in controlling polymorphism[9] and chirality.[10]

There has been a recent increase in the number of reports on the concept of nonclassical crystallization, which differs from the classical idea of layer-by-layer growth of crystals involving atomic or molecular building units.

A quarter of a century ago, solute clusters with an approximate diameter of 16 nm and their aggregates were observed in an aqueous solution of citric acid, indicating that the crystallization of citric acid monohydrate proceeds through the aggregation of clusters rather than through molecule-by-molecule growth.[11–13] In 2008, the existence was reported of well-defined clusters in a solution of calcium carbonate prior to its crystallization.[14] More-recent reports describe crystallization pathways from solution to crystals through mesoscopic intermediates that are metastable with respect to the mother liquid compared with the emerging crystalline phase,[15] ‘‘dense liquid’’ intermediates remaining in solution for many hours before sudden sedimentation of gold sulfide,[16] and the formation of aggregates derived from simple ions and ion pairs in aqueous

solutions prior to the nucleation of calcium carbonate.[17] Crystallization appears to proceed through aggregation of such clusters; that is, the cluster might be the smallest growth unit of a crystal.[18]

The concepts of NCC also have profound implications in latent-heat storage technologies that exploit the crystallization of phase-change materials, where supercooling causes severe problems.[19] When a high degree of supercooling is required to promote the crystallization of a cold-storage material, additional cooling energy is required, resulting in poor energy efficiency.[20]

When supercooled aqueous solutions of several latent-heat storage materials were examined by scanning electron microscopy using the freeze–fracture replica method, clusters with radii of about 5–10 nm were detected.[21–23] The relationship between cluster formation/aggregation and the degree of supercooling prior to crystallization indicated that clusters promote crystallization.[2] This suggests that the crystallization of latent-heat storage materials proceeds by an NCC process. The memory effect might result from the dissolution of crystals to form cluster units. We therefore examined the dissociation of a single crystal of tetra-*n*-butylammonium fluoride (TBAF) semiclathrate hydrate (SCH), a latent-heat storage material, by in-situ liquid-cell transmission electron microscopy [LC-TEM; See the Supplemental Information (SI) for the experimental procedures.].[8,24–28] Our results suggest the presence of a nonclassical "cluster-unit" dissolution process that might promote recrystallization.

2. RESULTS AND DISCUSSION

Overview of the Dissociation Processes under Electron-Beam Irradiation

We observed the dissociation processes of three tetragonal crystals (**Figures 1A**–**C** and **SI, Figures S1** and **S2**) and one cubic crystal (**Figures 1D**–**G**) under electron-beam irradiation (~5×10^4 electrons nm^{-2} s^{-1}). Although the cubic structure is the most stable crystal structure of

TBAF SCH, the incongruent-type dissociation temperature of tetragonal TBAF SCH (300.4 K) is only 0.5 K lower than that of the cubic form (300.9 K).[29]

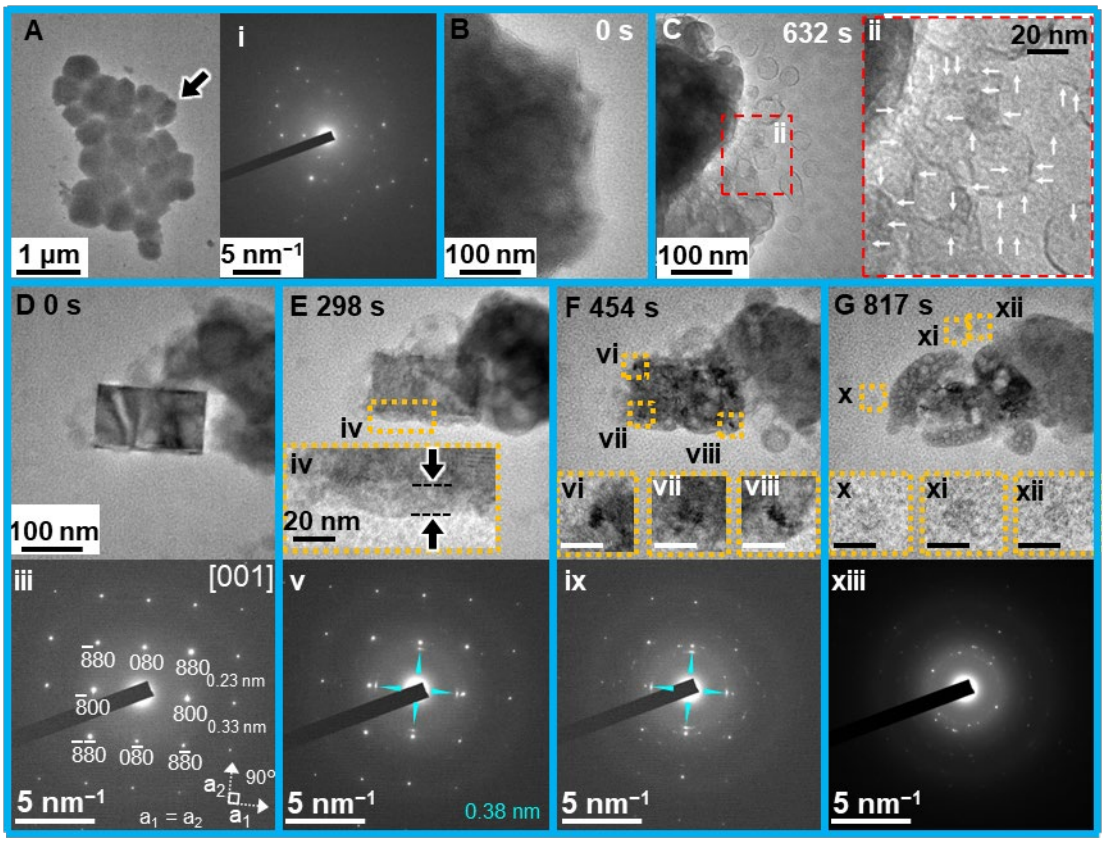

Figure 1. Dissociation processes of TBAF SCH crystals under electron irradiation. **A.** Bright-field TEM image of tetragonal crystals and the corresponding electron-diffraction pattern **i**. **B** and **C**. Enlarged images of the regions shown by an arrow in A at 0 s and 632 s, respectively. The timing started on increasing the electron dose rate to 5×10^4 electrons nm^{-2} s^{-1}. Inset **ii** shows an enlarged image of the red box region in C. White arrows show tiny particles with several nanometers in diameter. **D**–**G**. Bright-field TEM images at various times after initiation of electron-beam irradiation at 8×10^4 electron nm^{-2} s^{-1}. Insets **iii**, **v**, **ix**, and **xiii** are the electron-diffraction patterns corresponding to the TEM images in each blue box, obtained from the [001] direction. Enlarged

image **iv** shows the bright contrast region, indicated by arrows, that appeared on the surface of the crystal. Insets **vi**–**viii** and **x**–**xii** show clusters dissolved from the crystal. The cyan arrows in Insets **v** and **ix** show diffraction spots of 0.38 nm, attributed to an intermediate metastable phase in the dissociation process. The magnification for **E**–**G** is the same as that for **D**. The scale bars in Insets **vi**–**viii** and **x**–**xii** are 20 nm.

An aggregate of tetragonal crystals showed multiple diffraction spots (**Figure 1A**, Inset **i**), suggesting the presence of a collective of randomly oriented single crystals. Part of the aggregate of tetragonal crystals was magnified and the electron dose rate was increased from 10 to ~50,000 electron nm^{-2} s^{-1} (**Figure 1B**). On electron-beam irradiation, the outer periphery of the crystal appeared to dissociate with the release of two types of spherical object at 632 s (**Figure 1C**). One of these types of object had the characteristic contrast of a shell structure with a diameter of 20–40 nm and, in strong contrast, the other was a tiny particle measuring a few nanometers.

The tiny particles indicated by white arrows in Inset **ii** of **Figure 1C** were, at most, several nanometers in diameter and were probably clusters composed of TBAF SCH, which could promote recrystallization. Note that the movement and diffusion of solvent and solute molecules are prevented due to the confined space of a liquid cell. Then, clustering of dissociated molecules may be accelerated.[26] Whether the dissolution process accompanied by clusters observed in this study is a phenomenon that also occurs in conventional dissolution is a topic for the future. However, our observation results are consistent with previous reports that clusters promote the recrystallization of clathrate hydrates in general condition, [21–23] a phenomenon known as the

memory effect. In other words, the results of this direct observation support the hypothesis that clusters promote recrystallization.

The fresh cubic crystal at 0 s had a rectangular shape with sharp edges (**Figure 1D**). According to a crystallographic information file from Komarov et al.,[29] the corresponding electron-diffraction pattern (**Figure 1D,** Inset **iii**) is consistent with a single cubic crystal of space group $I\bar{4}3d$ (a = 24.37 Å) in the (001) orientation (except for the relative intensities of some spots), based on the extinction rule. The weak halo rings are attributable to two amorphous silicon nitride windows and/or the solution. The lattice spacing d_1 = 0.33 nm of the single crystal was assigned to be (800) based on the literature,[29] although the extinction rule is not fully satisfied.

After the start of electron-beam irradiation, additional diffraction spots attributed to a crystal with a 15% larger lattice constant appeared in the same crystallographic orientation at 298 s (**Figure 1E,** Inset **v**) suggesting the formation of a crystal as an intermediate phase during the dissociation. The crystal further dissociated and 10-nm-sized clusters were observed on the crystal surface at 454 s (**Figure 1F,** Insets **vi**–**viii**). The intensity of the original diffraction spots became weaker than that originating from the intermediate phase. In addition, many other diffraction spots appeared, indicating the progress of polycrystallization. Finally, the crystal totally lost its rectangular shape and, at 817 s, several spherical contrasts with sizes of less than 30 nm were observed surrounding it (**Figure 1G, Insets x**–**xii**). Despite the significant change in crystal shape, weak electron-diffraction spots originating from the initial cubic crystal remained visible (**Figure 1G,** Inset **xiii**), indicating that a part of the cubic crystal remained within the central area.

The polycrystallization observed in Figure 1G is likely influenced by both the presence of clusters and local saturation changes induced by electron-beam irradiation. The clusters formed during dissociation, facilitate the growth of new crystalline domains, which would contribute to

polycrystallization. This is consistent with previous studies on hydrate recrystallization, where clusters serve as precursors for rapid crystal growth.[23]

On the other hand, the electron beam induces radiolysis of water, leading to local fluctuations in solute concentration, which can create supersaturation zones around the dissolving crystal. These fluctuations can also promote polycrystallization independently.[26] Given the coexistence of these two factors, it is likely that polycrystallization results from a combination of cluster-mediated nucleation and saturation-driven crystallization.

Detailed Dissociation Process of a Cubic Single Crystal

During the dissociation process, we observed the generation and disappearance of moiré patterns in the TEM images (**Figure 2**). In Figure 2, the moiré patterns are highlighted by double circles; patterns identified as corresponding to the same moiré pattern on the basis of their position and size within the crystal are shown with the same color. Moiré patterns that were densely packed and could not be individually tracked are enclosed by white dashed circles. For example, the moiré patterns enclosed by red circles had a lifetime estimated to be between 146 s (**Figure 2C**) and 382 s (**Figure 2G**).

Figure 2A (0 s) shows the initial state of the single crystal just after electron-beam irradiation (~8×10^4 electrons nm^{-2} s^{-1}). In **Figure 2B** (103 s), slight distortions in the smoothness of the crystal facets appeared and faint moiré patterns began to emerge in the regions delineated by the white dashed circles.[30–33] In **Figure 2C** (146 s), clear moiré patterns can be observed in the areas enclosed by the circles, and their presence was supported by a fast Fourier transform (FFT) image (**Figure 2C**, Inset **i**). Later, moiré patterns were observed over the entire surface of the crystal, as indicated by the circles at 226 s (**Figure 2D**). The presence of moiré patterns was also supported

by the FFT images in **Figure 2**, Insets **iii** and **iv**. The diffraction spots (**Figure 2D,** Inset **ii**) indicate the presence of a single crystal, suggesting that the crystal structure was not significantly decomposed at 226 s.

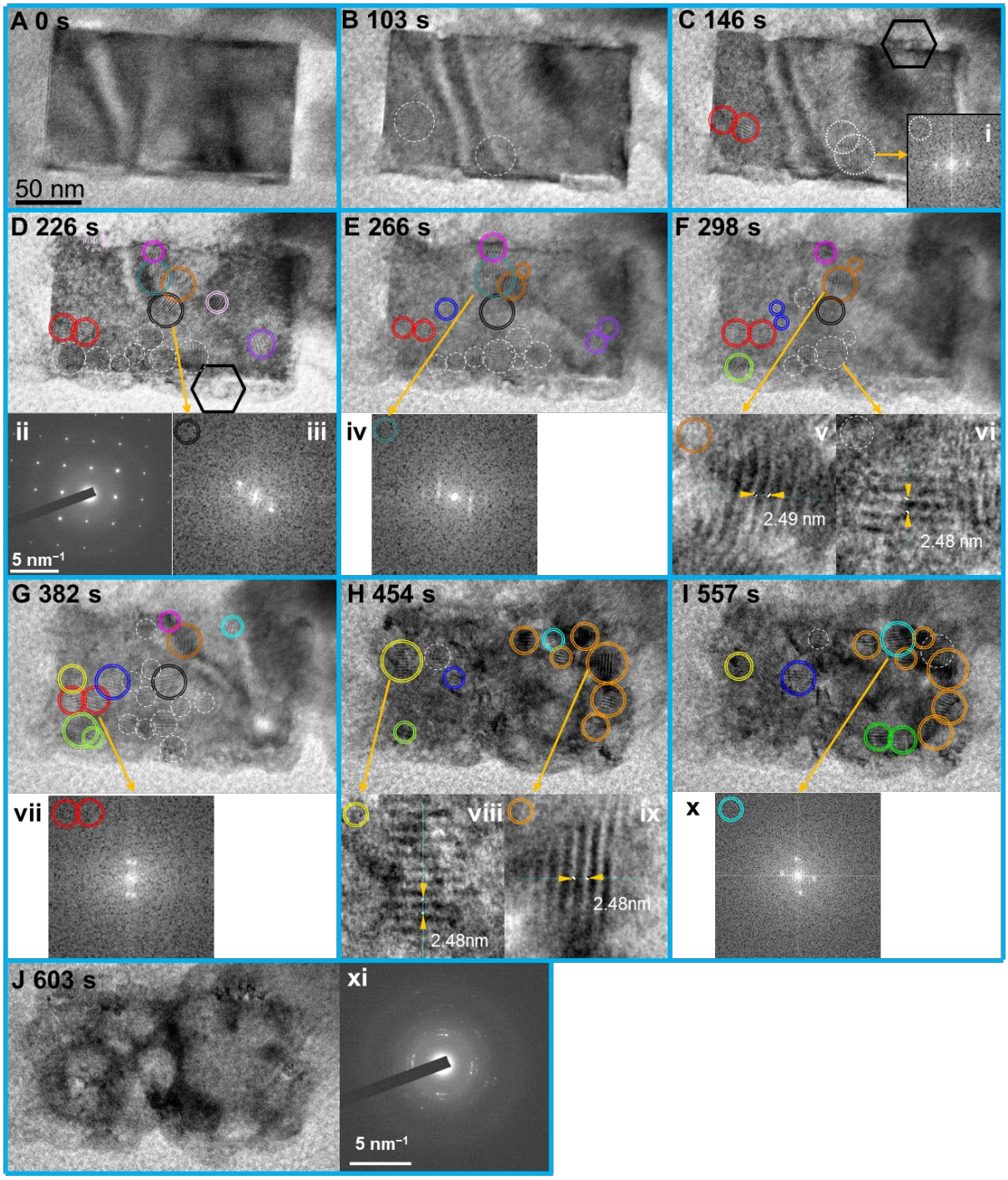

Figure 2. Detailed dissociation processes with the generation and disappearance of moiré patterns in a cubic TBAF SCH single crystal under electron-beam irradiation. **A**–**J**. Bright-field TEM images with time progress. Double circles indicate moiré patterns, and the same color was assigned to those determined to correspond to a single moiré pattern based on its position and size within the crystal. The white dashed circles indicate moiré patterns that were densely packed and could not be individually tracked. Insets **i**, **iii**, **iv**, **vi**, and **ix**. FFT images taken from selected regions indicated by circles in the upper-left-hand corner and the orange arrows. Insets **ii** and **ix**. Electron-diffraction pattern taken from the central part of the crystal. Insets **v**, **vi**, **viii**, and **ix**. Enlarged images of the regions indicated by circles in the upper-left-hand corner and the orange arrows. Contrast profiles along the blue lines are presented in the SI, Figure S3.

Moiré patterns were continuously observed in the TEM image until 557 s (**Figure 2I**). The moiré periodicities observed in the TEM images were determined to be 2.48–2.49 nm (Insets **v, vi**, **viii**, and **ix** in **Figure 2,** and **SI, Figure S3**). Based on the diffraction spots in **Figures 1E** and **1F** and **SI, Figure S3**, the lattice spacings were assigned as $d_1 = 0.33$ nm and $d_2 = 0.38$ nm.

Assuming parallel moiré patterns, we can apply the following equation:

$$D = (d_1 \times d_2)/(d_1 - d_2) \qquad (1)$$

where D is the moiré periodicity, d_1 is the lattice spacing of the single crystal (0.33 nm), and d_2 is the lattice spacing of the newly appearing crystal that produced the moiré pattern. From Equation 1, the moiré periodicity D was calculated to be 2.5 nm, which is in good agreement with the observed results from the TEM images (**Figure 2**, Insets **v**, **vi**, **viii,** and **ix** and **SI, Figure S3**). We can then conclude that the moiré patterns generated during the crystal dissociation under electron-beam irradiation result from interference between the initial lattice spacing of 0.33 nm and a lattice

spacing of 0.38 nm produced after the generation of the moiré pattern (**Fig. 3**). Unlike moiré fringes caused by strain-induced distortions, which are typically localized to a few atomic layers. The persistence and spatial extent of the observed moiré patterns suggest that the intermediate phase forms a relatively thick layer on the mother crystal, maintaining a coherent but distinct lattice structure. The presence of a stable, well-defined periodicity in the moiré pattern indicates that this intermediate phase is not merely an amorphous transition layer but retains a crystalline nature, leading to long-range interference effects between the two lattices.

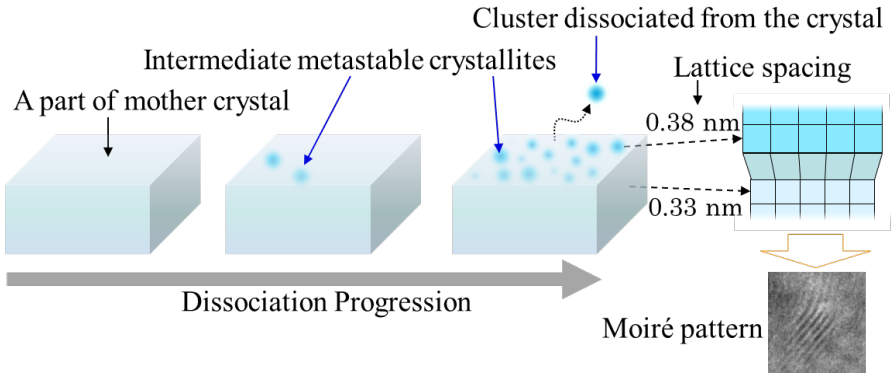

Figure 3. Schematic of the nonclassical "cluster-unit" dissociation process of TBAF SCH.

In the dissociation process, bubble-like shapes are observed at the same time as the formation of moiré fringes. If moiré fringes were formed by an interaction between the bubble-shaped crystals and the mother crystal, moiré fringes should be observed surrounding the area where there is no moiré fringe corresponding to the center of the bubble. However, the moiré fringes always appear homogeneously. In addition, bubble-like shapes do not show diffraction contrasts or lattice images originating from crystal. Therefore, it can be concluded that the formation of moiré fringes, i.e. the

dissociation process accompanied by clusters, is independent to the formation of bubble-like substances due to electron beam irradiation.

The crystal dissociation under electron-beam irradiation occurred not only on the crystal surface parallel to the substrate, but also on the side surfaces. The crystal's side surfaces were smooth in **Figure 2A**, but the smoothness was gradually lost on electron-beam irradiation. Each side surface had a significantly brighter contrast layer with a thickness of 15–20 nm (**Figure 1E,** Inset **iv**). In addition, regions about 15 nm in size appeared with relatively strong contrasts (**Figures 2B**–**2D**), especially on the lower and upper side surfaces. Examples are indicated by the hexagons in **Figures 2C** and **2D**.

The formation of moiré patterns observed in this study is attributed to interference between the initial cubic lattice of the mother crystal and an overlying intermediate phase with a slightly different lattice spacing. Given that the moiré periodicity (2.48–2.49 nm) is significantly larger than the underlying lattice constants (0.33 nm and 0.38 nm), the intermediate phase must maintain a relatively consistent thickness to sustain the observed moiré contrast.

This phenomenon suggests that the intermediate phase does not simply form and dissolve randomly but instead undergoes a well-defined transition before detaching as clusters. Unlike strain-induced moiré effects, which are usually limited to a few atomic layers, the persistence and spatial uniformity of the observed moiré patterns indicate that the intermediate phase maintains a coherent crystalline structure over an extended thickness. Such behavior is consistent with previous studies on metastable crystalline overlayers in phase-transition processes.[15] The disappearance of moiré patterns as dissolution progresses further supports the notion that they originate from an ordered intermediate phase rather than from random lattice distortions.

The appearance of the moiré patterns (enclosed by circles and color-coded based on size in blue, cyan, red, pink, and green, representing 10, 15, 20, 25, 30 nm Φ, respectively) is shown in **SI, Figure S4**. The judgment regarding the moiré patterns was made by enlarging the TEM images and identifying the presence of three or more parallel lines.

The size distribution of the regions containing moiré patterns is shown in **Figure 4**. The dissociation of the single crystal due to electron irradiation proceeded at the level of units with a size in the range 10–30 nm with a mode diameter of 15.0 nm and a median diameter of 19.3 nm. This size distribution is consistent with the size of clusters observed around the single crystal in the enlarged TEM images of Insets **vi**–**viii** and **x–xii** in **Figures 1F** and **1G**.

This size distribution is consistent with the size of clusters observed around the single crystal, suggesting a direct correlation between the formation of the moiré patterns and the cluster-mediated dissolution process.

The observed moiré patterns are indicative of an intermediate crystalline phase with a finite thickness on the mother crystal. As the dissolution progresses, this intermediate phase detaches in discrete units, leading to the formation of the observed clusters. The disappearance of moiré patterns coincides with the separation of these intermediate-phase clusters, supporting the hypothesis that the moiré contrast arises from a structured overlayer rather than from localized strain effects.

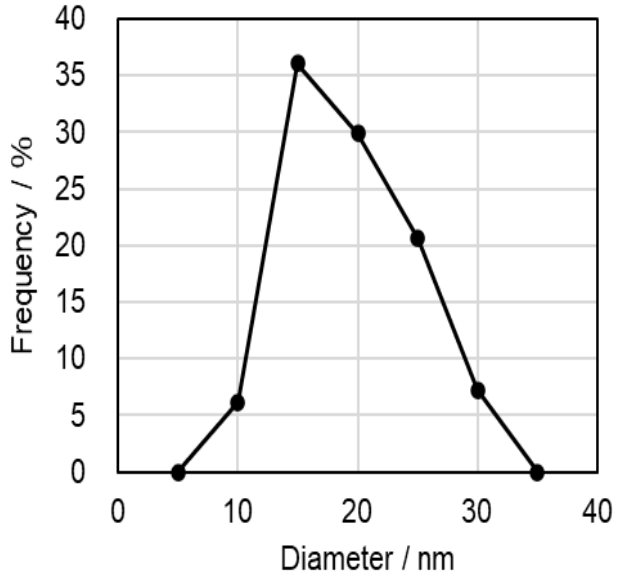

Figure 4. The size distribution of the moiré regions observed in the dissociation process of the cubic crystal in Figure 2 and SI, Figure S4.

On electron-beam irradiation, the single crystal undergoes dissociation, along with the generation of moiré patterns, where the surface expands in units of 30 nm or less that peel off from the deeper layers, eventually decomposing through polycrystallization. The 30-nm-sized units might correspond to the particles shown in **Figure 1G,** Insets **x**–**xii**.

The lifetime of moiré patterns was investigated (**Figure 5**) and shown to have a mode value of 2.0 minutes and a median value of 2.3 minutes at an electron dose rate of 8×10^4 electron nm^{-2} s^{-1}. In terms of the electron dose, the lifetime of moiré patterns during crystal dissociation was determined to be 1×10^7 electron nm^{-2}. The lifetime of the moiré patterns is regarded as corresponding to the lifetime of the intermediate metastable crystallites during the dissociation of the single crystal. There are two possible causes of dissociation by electron-beam irradiation: a kinetic process acting on molecules in the crystal or environmental changes due to radiolysis of

the solution. It has been reported that the damage to crystals caused by electron-beam irradiation is mainly the result of amorphization rather than molecular decomposition.[34] Amorphization promotes dissolution because amorphous materials have a higher solubility than the corresponding crystal. The dissolution process observed in this study involves intermediate metastable crystallites 10–30 nm in size, which is different from the dissolution process accompanied by amorphization due to random molecular orientation. The temperature increase due to the electron dose rate (~5-8×10^4 electrons nm^{-2} s^{-1}) used in our experiment is estimated to be 2-3 K.[35] When compared to the decomposition temperature of SCH (300.9 K) in TBAF, the ambient temperature is 293 K, so even if the temperature increases by 3 K, it will still be lower than the decomposition temperature. Therefore, we conclude that the main cause of crystal dissociation is the undersaturation of the solution environment for the crystal due to radiolysis of the solution by electron-beam irradiation rather than local temperature increases.

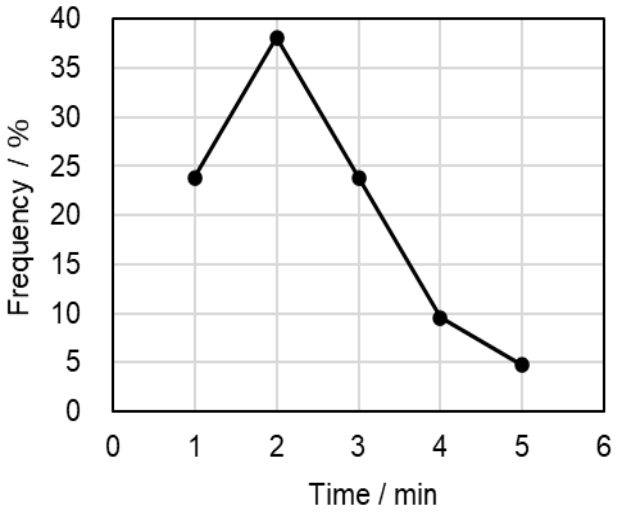

Figure 5. The lifetime of moiré patterns from generation to disappearance in the cubic crystal observed in Figure 2 and SI, Figure S4.

CONCLUSION

TEM observations enabled the visualization of the dissociation processes of TBAF SCH single crystal, which progresses with repeated generation and disappearance of moiré patterns. This corresponds to the formation of intermediate metastable crystallites [15 nm (mode) and 19.3 nm (median)] on the crystal surface and is discrete. Particles of a similar size were observed around the dissociating crystals. These particles correspond to clusters of TBAF SCH, which are reported to be responsible for the easy recrystallization of TBAF SCH crystals, a phenomenon known as the memory effect.[21–23] In the future, we expect that knowledge relating to the formation of clusters could lead to the development of an efficient latent-heat storage technology with a reduced cooling energy.

ASSOCIATED CONTENT

Supporting Information.

Materials and solution preparation, TEM and the liquid cell, time-resolved LC-TEM observations, and four supporting figures.

AUTHOR INFORMATION

Corresponding Author

*Yuki Kimura: Institute of Low Temperature Science, Hokkaido University, Kita-19, Nishi-8, Kita-ku, Sapporo 060-0819, Japan; E-mail: ykimura@lowtem.hokudai.ac.jp

Author Contributions

H.M., T.S., and Y.K. conceived the research idea. H.H., T.U., and T.Y. performed the TEM observations and analyzed the data. H.M. and T.S. summarized the research results and wrote the manuscript together with Y.K. after discussion with and input from all the coauthors.

Funding Sources

H.M. and T.S. gratefully acknowledge financial support from the Thermal Management Materials and Technology Research Association (TherMAT) project (JPNP15007), commissioned by the New Energy and Industrial Technology Development Organization (NEDO). TEM work was partly supported by Grant-in-Aids for Scientific Research (S) from JSPS KAKENHI (15H05731 and 20H05657).

ABBREVIATIONS

NCC, nonclassical crystallization; TBAB, tetra-n-butylammonium bromide; SCH, semiclathrate hydrate; TBAF, tetra-n-butylammonium fluoride; LC-TEM, liquid-cell transmission electron microscopy.

REFERENCES

(1) Kim, J.; Kimura, Y.; Puchala, B.; Yamazaki, T.; Becker, U.; Sun, W. Dissolution Enables Dolomite Crystal Growth Near Ambient Conditions. *Science* **2023**, *382*, 915–920.

(2) Machida, H.; Sugahara, T.; Masunaga, H.; Hirasawa, I. Calorimetric and Small-Angle X-Ray Scattering Studies on the Memory Effect in the Tetra-*n*-butylammonium Bromide Semiclathrate Hydrate System. *J. Cryst. Growth* **2020**, *533*, 125476.

(3) Nagao, H.; Ichiji, M.; Hirasawa, I. Synthesis of Platinum Nanoparticles by Reductive Crystallization Using Polyethyleneimine. *Chem. Eng. Technol.* **2017**, *40*, 1242–1246.

(4) Ike, Y.; Hirasawa, I. Polymorph Control of *L*-ArgHCl on Antisolvent Crystallization by Ultrasonic Irradiation. *Chem. Eng. Technol.* **2017**, *40*, 1318–1322.

(5) Kodera, T.; Kobari, M.; Hirasawa, I. Modeling and Growth Kinetics of Antisolvent Crystallization Applied to the Pharmaceutical Industry. *Chem. Eng. Technol.* **2019**, *42*, 1458–1465.

(6) Erdemir, D.; Lee, A. Y.; Myerson, A. S. Nucleation of Crystals from Solution: Classical and Two-Step Models. *Acc. Chem. Res.* **2009**, *42*, 621–629.

(7) Li, D.; Zhou, H.; Honma, I. Design and Synthesis of Self-Ordered Mesoporous Nanocomposite Through Controlled In-Situ Crystallization. *Nat. Mater.* **2004**, *3*, 65–72.

(8) Kimura, Y. Direct Observation of the Moment of Nucleation from a Solution by TEM. *Microscopy* **2021**, *7*, 13–21.

(9) Kimura, Y.; Niinomi, H.: Tsukamoto, K.; García-Ruiz, J. M. In Situ Live Observation of Nucleation and Dissolution of Sodium Chlorate Nanoparticles by Transmission Electron Microscopy. *J. Am. Chem. Soc.* **2014**, *136*, 1762–1765.

(10) Uwaha, M.; Katsuno, H. Mechanism of Chirality Conversion of Crystals by Viedma Ripening and Temperature Cycling. *J. Cryst. Growth* 2022, *598*, 126873.

(11) Ohgaki, K.; Makihara, Y.; Morishita, M.; Ueda, M.; Hirokawa, N. Solute Clusters in Aqueous Citric Acid Solutions. *Chem. Eng. Sci.* **1991**, *46*, 3283–3287.

(12) Ohgaki, K.; Hirokawa, N.; Ueda, M. Heterogeneity in Aqueous Solutions: Electron Microscopy of Citric Acid Solutions. *Chem. Eng. Sci.* **1992**, *47*, 1819–1823.

(13) Ueda, M.; Hirokawa, N.; Harano, Y.; Moritoki, M.; Ohgaki, K. Change in Microstructure of an Aqueous Citric Acid Solution under Crystallization. *J. Cryst. Growth* **1995**, *156*, 261–266.

(14) Gebauer, D.; Völkel, A.; Cölfen, H. Stable Prenucleation Calcium Carbonate Clusters. *Science* **2008**, *322*, 1819–1822.

(15) Sleutel, M.; Van Driessche, A. E. S. Role of Clusters in Nonclassical Nucleation and Growth of Protein Crystals. *Proc. Natl. Acad. Sci. U. S. A.* **2014**, *111*, E546–E553.

(16) Mikhlin, Y.; Karacharov, A.; Likhatski, M.; Podlipskaya, T.; Zizak, I. Direct Observation of Liquid Pre-Crystallization Intermediates During the Reduction of Aqueous Tetrachloroaurate by Sulfide Ions. *Phys. Chem. Chem. Phys.* **2014**, *16*, 4538–4543.

(17) Henzler, K.; Fetisov, E. O.; Galib, M.; Baer, M. D.; Legg, B. A.; Borca, C.; Xto, J. M.; Pin, S.; Fulton, J. L.; Schenter, G. K.; Govind, N.; Siepmann, J. I.; Mundy, C. J.; Huthwelker, T.; De Yoreo, J. J. Supersaturated Calcium Carbonate Solutions Are Classical. *Sci. Adv.* **2018**, *4*, eaao6283.

(18) Ishizuka, S.; Kimura, Y.; Yokoi, S.; Yamazaki, T.; Sato, R.; Hama, T. Self-Assembly of MoO_3 Needles in Gas Current for Cubic Formation Pathway. *Nanoscale* **2017**, *9*, 10109–10116.

(19) Wei, L.; Ohsasa, K. Supercooling and Solidification Behavior of Phase Change Material. *ISIJ Int.* **2010**, *50*, 1265–1269.

(20) Sharma S. D.; Sagara, K. Latent Heat Storage Materials and Systems: A Review. *Int. J. Green Energy* **2005**, *2*, 1–56.

(21) Machida, H.; Sugahara, T.; Hirasawa, I. Relationship Between Supercooling Stability and Solution Structure in Sodium Acetate Aqueous Solution. *J. Cryst. Growth* **2017**, *475*, 295–299.

(22) Machida, H.; Sugahara, T.; Hirasawa, I. Memory Effect in Tetra-*n*-butylammonium Bromide Semiclathrate Hydrate Reformation: The Existence of Solution Structures After Hydrate Melting. *CrystEngComm* **2018**, *20*, 3328–3334.

(23) Machida, H.; Sugahara, T.; Hirasawa, I. The Moment of Initial Crystallization Captured on Functionalized Nanoparticles. *Commun Mater.* **2021**, *2*, 66.

(24) Yamazaki, T.; Driessche, A.; Kimura, Y. High Mobility of Lattice Molecules and Defects During the Early Stage of Protein Crystallization. *Soft Matter*, **2020**, *16,* 1955–1960.

(25) Katsuno, H.; Kimura, Y.; Yamazaki, T.; Takigawa, I. Early Detection of Nucleation Events from Solution in LC-TEM by Machine Learning. *Front. Chem.* **2022**, *10*, 818230.

(26) Kimura, Y.; Katsuno, H.; Yamazaki, T. Possible Embryos and Precursors of Crystalline Nuclei of Calcium Carbonate Observed by Liquid-Cell Transmission Electron Microscopy. *Faraday Discuss.* **2022**, *235*, 81–94.

(27) Yamazaki, T.; Kimura, Y.; Vekilov. P. G.; Furukawa, E.; Shirai, M.; Matsumoto, H.; Van Driessche, A. E. S.; Tsukamoto, K. Two Types of Amorphous Protein Particles Facilitate Crystal Nucleation. *Proc. Natl. Acad. Sci. U. S. A.* **2017**, *114*, 2154–2159.

(28) Yamazaki, T.; Yashima, Y.; Katsuno, H.; Miyazaki, H.; Gondo, T.; Kimura, Y. In Situ Transmission Electron Microscopy Study of Bubble Behavior Near the Surface of Ice Crystals by Using a Liquid Cell with a Peltier Cooling Holder. *Microsc. Microanal.* **2023**, *29*, 1940–1949.

(29) Komarov, V. Y.; Rodionova, T. V.; Terekhova, I. S.; Kuratieva. N. V. The Cubic Superstructure-I of Tetrabutylammonium Fluoride $(C_4H_9)_4NF \cdot 29.7H_2O$ Clathrate Hydrate. *J. Inclusion Phenom. Macrocyclic Chem*. **2007**, 59, 11–15.

(30) Su, D.; Zhu, Y. Scanning Moiré Fringe Imaging by Scanning Transmission Electron Microscopy. *Ultramicroscopy* **2010**, *110*, 229-233.

(31) Denneulin, T.; Rouviere, J. L.; Béché, A.; Py, M.; Barnes, J. P.; Rochat, N.; Hartmann, J. M.; Cooper, D. The Reduction of the Substitutional C Content in Annealed Si/SiGeC Superlattices Studied by Dark-Field Electron Holography. *Semicond. Sci. Technol.* **2011**, *26*, 125010.

(32) Kim, S.; Lee, S.; Oshima, Y.; Kondo, Y.; Okunishi, E.; Endo, N.; Jung, J.; Byun, G.; Lee, S.; Lee, K. Scanning Moiré Fringe Imaging for Quantitative Strain Mapping in Semiconductor Devices. *Appl. Phys. Lett.* **2013,** *102*, 161604.

(33) Wang, Q. H.; Ri, S.; Tsuda, H.; Kodera, M.; Suguro, K.; Miyashita, N. Visualization and Automatic Detection of Defect Distribution in GaN Atomic Structure from Sampling Moiré phase. *Nanotechnology* **2017,** *28*, 455704.

(34) Liu, D.; Fu, J.; Elishav, M.; Yamamouchi, K.; Hirshberg, B.; Nakamuro, T.; Nakamura, E. Melting Entropy of Crystals Determined by Electron-Beam–Induced Configurational Disordering. *Science* **2024,** *384*, 1212–1219.

(35) Grogan, J. M; Schneider, N. M; Ross, F. M; Bau, H. H. Bubble and pattern formation in liquid induced by an electron beam. *Nano Lett.* **2014**, *14*, 359–364.